

Stellar Scintillation and the Atmosphere's Vertical Turbulence Profile

July 2001

Prepared by

J. C. CAMPARO
Electronics & Photonics Laboratory
Laboratory Operations

Prepared for

SPACE AND MISSILE SYSTEMS CENTER
AIR FORCE MATERIEL COMMAND
2430 E. El Segundo Boulevard
Los Angeles Air Force Base, CA 90245

Contract No. F04701-93-C-0094

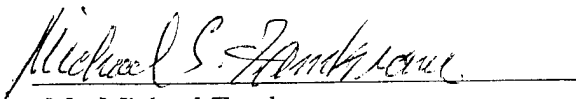
Engineering and Technology Group

APPROVED FOR PUBLIC RELEASE;
DISTRIBUTION UNLIMITED

This report was submitted by The Aerospace Corporation, El Segundo, CA 90245-4691, under Contract No. F04701-93-C-0094 with the Space and Missile Systems Center, 2430 E. El Segundo Blvd., Los Angeles Air Force Base, CA 90245. It was reviewed and approved for The Aerospace Corporation by L. T. Greenberg, Vice President, Laboratory Operations. Mr. Michael Zambrana was the project officer for the Mission-Oriented Investigation and Experimentation (MOIE) program.

This report has been reviewed by the Public Affairs Office (PAS) and is releasable to the National Technical Information Service (NTIS). At NTIS, it will be available to the general public, including foreign nationals.

This technical report has been reviewed and is approved for publication. Publication of this report does not constitute Air Force approval of the report's findings or conclusions. It is published only for the exchange and stimulation of ideas.

A handwritten signature in cursive script, reading "Michael S. Zambrana", is written over a horizontal line.

Mr. Michael Zambrana
SMC/AXE

REPORT DOCUMENTATION PAGE			Form Approved OMB No. 0704-0188	
Public reporting burden for this collection of information is estimated to average 1 hour per response, including the time for reviewing instructions, searching existing data sources, gathering and maintaining the data needed, and completing and reviewing the collection of information. Send comments regarding this burden estimate or any other aspect of this collection of information, including suggestions for reducing this burden to Washington Headquarters Services, Directorate for Information Operations and Reports, 1215 Jefferson Davis Highway, Suite 1204, Arlington, VA 22202-4302, and to the Office of Management and Budget, Paperwork Reduction Project (0704-0188), Washington, DC 20503.				
1. AGENCY USE ONLY (Leave blank)		2. REPORT DATE July 2001		3. REPORT TYPE AND DATES COVERED
4. TITLE AND SUBTITLE Stellar Scintillation and the Atmosphere's Vertical Turbulence Profile			5. FUNDING NUMBERS F04701-93-C-0094	
6. AUTHOR(S) J. C. Camparo				
7. PERFORMING ORGANIZATION NAME(S) AND ADDRESS(ES) The Aerospace Corporation Technology Operations El Segundo, CA 90245			8. PERFORMING ORGANIZATION REPORT NUMBER TR-2000(8555)-6	
9. SPONSORING/MONITORING AGENCY NAME(S) AND ADDRESS(ES) Space and Missile Systems Center Air Force Materiel Command 2430 E. El Segundo Blvd. Los Angeles Air Force Base, CA 90245			10. SPONSORING/MONITORING AGENCY REPORT NUMBER SMC-TR-02-04	
11. SUPPLEMENTARY NOTES				
12a. DISTRIBUTION/AVAILABILITY STATEMENT Approved for public release; distribution unlimited			12b. DISTRIBUTION CODE	
13. ABSTRACT (Maximum 200 words) The relationship between stellar scintillation in the strong-focusing regime and the atmosphere's vertical turbulence profile is investigated with numerical simulation. For two distinct atmospheric profiles, the irradiance variance at a point on a telescope aperture is evaluated as a function of the weighted path-integrated turbulence (i.e., Rytov variance). Additionally, we compute the aperture-averaged irradiance variance and the log-amplitude correlation across the aperture as functions of the Rytov variance. For one atmospheric profile, scintillation is dominated by turbulence in the tropopause; for the other, scintillation arises from turbulence in both the tropopause and the lower troposphere. The numerical results indicate that (1) stellar scintillation depends on the actual profile of atmospheric turbulence and not just on its weighted integral, and (2) in the strong-focusing regime the irradiance variance is determined primarily by an optical wave's coherence length as it passes through the tropopause.				
14. SUBJECT TERMS scintillation, atmospheric turbulence, optical propagation			15. NUMBER OF PAGES 10	
			16. PRICE CODE	
17. SECURITY CLASSIFICATION OF REPORT UNCLASSIFIED	18. SECURITY CLASSIFICATION OF THIS PAGE UNCLASSIFIED	19. SECURITY CLASSIFICATION OF ABSTRACT UNCLASSIFIED	20. LIMITATION OF ABSTRACT	

Contents

1. Introduction.....	3
2. Vertical Profiles of Atmospheric Turbulence and the Numerical Procedure.....	3
3. Results.....	5
4. Discussion.....	6
5. Summary.....	6
Appendix A.....	7
Acknowledgments.....	8
References and Notes.....	8

Figures

1. $C_n^2(h)h^{5/6}$ versus altitude for the Hufnagel-Valley model of atmospheric turbulence.....	4
2. Circles, log-amplitude correlation function for the HV-21 model with $\Gamma = 1$ (i.e., weak turbulence): $r_o = 11.8$ cm, and $\sigma_R^2 = 0.11$	5
3. Phase-screen calculation of irradiance variance σ_I^2 versus the Rytov standard deviation σ_R	5
4. Phase-screen calculation of the aperture-averaged irradiance variance $\langle \sigma_I^2 \rangle$ versus the Rytov standard deviation σ_R	5
5. Log amplitude correlation function $B_x(\rho) / B_x(0)$ in the strong-focusing regime.....	5
6. Rytov variance parameterized by the scintillation parameter f as discussed in the text.	6

Tables

1. Altitudes of Phase Screens	7
-------------------------------------	---

1. INTRODUCTION

Stellar scintillation, defined here generally as the intensity fluctuations of a plane wave after propagating from space to Earth, is typically quantified in terms of the irradiance variance at a point on a telescope aperture, $\sigma_I^2 = \langle I^2 \rangle / \langle I \rangle^2 - 1$.¹ In the regime of weak turbulence (i.e., $\sigma_I^2 < 1$), scintillation is well understood and described by Rytov's theory, where σ_I^2 just depends on the total altitude-weighted turbulence along the propagation path²:

$$\sigma_I^2 \cong \sigma_R^2 \cong \exp \left[2.25 k^{7/6} \sec^{11/6}(\phi) \int_0^\infty C_n^2(h) h^{5/6} dh \right] - 1. \quad (1)$$

Here the refractive index structure constant $C_n^2(h)$ is a measure of turbulence strength at altitude h , ϕ is the zenith angle, and k is the optical wave vector's magnitude. However, in the regime of strong turbulence it is well known that the relationship between σ_I^2 and σ_R^2 breaks down. Specifically, for $\sigma_I^2 > 1$ the irradiance variance saturates, that is, it reaches a peak (referred to as the strong-focusing regime) and then slowly decreases with increasing total turbulence.³

Over the past decade considerable progress has been made in understanding the saturation of scintillation, in particular for horizontal propagation through homogeneous turbulence. For example, the role of the inner scale has been elucidated⁴ and has been found to have a greater significance for spherical waves than for plane waves.⁵ Additionally, the probability density function of irradiance has been numerically evaluated, and its deviations from a log-normal distribution have been studied.⁶ The situation is quite different with regard to stellar scintillation, however, where very little is known about saturation. In large part this is because the irradiance vari-

ance typically associated with stellar scintillation is small enough that Rytov's theory applies.⁷ Nevertheless, deviations from Rytov's theory can occur, especially at large zenith angles,⁸ and so it is reasonable to question how the saturation of stellar scintillation might differ from that associated with propagation through homogeneous turbulence. In particular, since expression (1) is no longer valid in the case of saturation, one might wonder whether σ_I^2 still depends on just the integrated turbulence along the entire propagation path or whether certain atmospheric regions play different roles in producing scintillation.

In the following sections, we consider this question by numerically simulating optical propagation through two distinct profiles of atmospheric turbulence. For one profile scintillation is dominated by turbulence in the tropopause, while for the other both tropopause and low-altitude tropospheric turbulence contribute to scintillation. In Section 2 we briefly discuss the numerical simulation procedure and our vertical profiles of atmospheric turbulence. The results are presented in Section 3, where the combination of high- and low-altitude turbulence is shown to be more effective in producing scintillation in the strong-focusing regime than high-altitude turbulence alone. In Section 4 we explain this result by considering the relationship between a propagated field's lateral coherence length and its Fresnel length for the two different atmospheric profiles.

2. VERTICAL PROFILES OF ATMOSPHERIC TURBULENCE AND THE NUMERICAL PROCEDURE

To describe the atmosphere's vertical turbulence profile, we employ a slightly modified version of the Hufnagel-Valley (HV) model¹:

$$C_n^2(h) = \Gamma \{ 8.15 \times 10^{-56} v_s^2 h^{10} \exp[-(h/1000)] + 2.7 \times 10^{-16} \exp[-(h/1500)] + A \exp[-(h/100)] \}. \quad (2)$$

Here v_s is a parameter in meters per second that controls high-altitude turbulence, and A accounts for boundary-layer atmospheric turbulence. (In the literature, v_s is sometimes defined as the rms wind speed in the 5–20-km altitude range.¹) Γ is a factor that scales a particular profile to higher and lower levels of turbulence and simultaneously could account for the $\sec^{1/6}(\phi)$ zenith-angle factor in expression (1).

A particular profile of turbulence that is often used in studies of optical propagation through the atmosphere is the HV-21 profile: $v_s = 21$ m/s and $A = 1.7 \times 10^{-14} \text{ m}^{-2/3}$. Here, we examine this profile's influence on the saturation of scintillation by increasing Γ for a 1- μm reference wavelength. In this way, we keep the relative shape of the profile constant, while increasing the level of integrated turbulence (i.e., σ_R^2). The altitude-weighted contribution of the HV-21 profile to stellar scintillation [i.e., $C_n^2(h)h^{5/6}$] is shown in Fig. 1 for the specific case of $\sigma_R^2 = 0.5$, and it is apparent that both high-altitude (~ 11 km) and low-altitude (~ 1.4 km) turbulence contribute to scintillation.⁹ For comparative purposes, we have also considered a profile that we refer to as the high-altitude (HA) profile. For the HA profile, $\Gamma = 1$, and v_s is varied to produce different levels of turbulence; A is somewhat arbitrarily set to $1.0 \times 10^{-13} \text{ m}^{-2/3}$. Though the HA profile may appear somewhat artificial, as will be seen it provides a good countertype for the more realistic HV-21 profile. Basically, the idea behind the HA profile is to have a point of comparison that will allow us to better understand those features of a turbulence profile that play a significant role in stellar scintillation. The HA's altitude-weighted contribution to stellar scintillation is also shown in Fig. 1 for the case of $\sigma_R^2 = 0.5$, and it is clear that scintillation in this case is influenced primarily by turbulence in the tropopause.

Propagation through the turbulent atmosphere is studied numerically according to standard methodology.^{10,11} Briefly, we simulate three-dimensional wave propagation

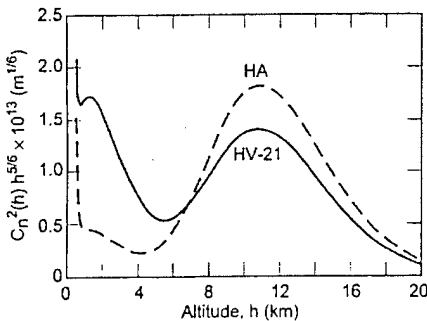


Fig. 1. $C_n^2(h)h^{5/6}$ versus altitude for the Hufnagel–Valley model of atmospheric turbulence. For the HV-21 profile, $A = 1.7 \times 10^{-14} \text{ m}^{-2/3}$, $v_s = 21$ m/s, and the strength of turbulence is varied by changing Γ (for the graph $\Gamma = 3.85$). For the high-altitude profile, labeled HA, $A = 1.0 \times 10^{-13} \text{ m}^{-2/3}$, $\Gamma = 1$, and the strength of turbulence is varied by changing the rms wind speed (for the graph $v_s = 47$ m/s). Each profile shown in the figure yields $\sigma_R^2 = 0.5$.

by placing a number, N_s , of thin random-phase screens at specific altitudes, h_i . Prior to impinging on the i th phase screen, the optical field $E(\rho, h_i^-)$ is given by

$$E(\rho, h_i^-) = E_o(\rho, h_i^-) \exp[i\phi(\rho, h_i^-)], \quad (3)$$

where ρ is a position vector in a plane perpendicular to the propagation direction (for the computations, the zenith angle is zero), and where E_o and ϕ are real scalar fields. The phase screen imparts an additional random phase to this wave θ (where the statistical properties of θ are determined by the characteristics of turbulence at h_i), so that after propagation through the phase screen, the field becomes $E(\rho, h_i^+) = E_o(\rho, h_i^-) \exp[i\{\phi(\rho, h_i^-) - \theta(\rho, h_i^-)\}]$. Taking the two-dimensional Fourier transform of $E(\rho, h_i^+)$, the field is propagated to the next screen under the Fresnel approximation,¹² and after an inverse Fourier transform this becomes $E(\rho, h_{i+1}^-)$. We start from an initial monochromatic plane wave at an altitude of 20 km, and the wave is propagated to a telescope aperture on the Earth's surface. More details on the numerical simulation may be found in Appendix A.

A single realization consisted of plane-wave propagation ($\lambda = 1 \mu\text{m}$) from the lower stratosphere to the Earth through four 512×512 pixel phase screens of equal length. Depending on the simulation parameters, the phase-screen lengths ranged from 170 to 210 cm.¹³ For each simulation, we recorded the field intensity at the central pixel of a 25-cm-diameter telescope aperture,¹⁴ and we determined the product of the central pixel's log amplitude with the log amplitude of all other aperture pixels. Additionally, we determined the aperture-averaged intensity of the propagated field for each simulation. A single computational run involved 3000 realizations of atmospheric propagation, and four to seven runs were used to generate pooled estimates¹⁵ of irradiance variance. The log-amplitude correlation functions were evaluated from a single computational run of 15,000 realizations. Though one could attempt to calculate σ_I^2 using fewer simulations (for example, by treating each pixel from a single realization as a separate estimate of the intensity fluctuations), we chose a different approach, since the intensity fluctuations of neighboring pixels are correlated. Calculations were performed on a dual-processor 600-MHz DEC Alpha Server 4000, and a single realization required ~ 18 s.

As evidence of the numerical procedure's validity, Fig. 2 shows the log-amplitude correlation function [i.e., $B_x(\rho)/B_x(0)$] for the case of HV-21 turbulence with $\Gamma = 1$. Since the turbulence is relatively weak in this case (i.e., $\sigma_R^2 = 0.11$), the numerical results may be compared with Rytov theory, where

$$B_x(\rho) = 4\pi^2 k^2 \int_0^H C_n^2(h) \left[(0.033) \int_0^\infty J_0(\kappa\rho) \kappa^{(-11/3)} \times \sin^2\left(\frac{\kappa^2 h}{2k}\right) \kappa d\kappa \right] dh. \quad (4)$$

In writing Eq. (4), we have restricted ourselves to Kolmogorov turbulence. The solid curve in Fig. 2 corresponds to the prediction of Eq. (4), and as one would ex-

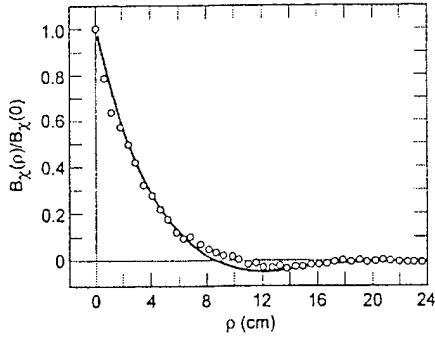


Fig. 2. Circles, log-amplitude correlation function for the HV-21 model with $\Gamma = 1$ (i.e., weak turbulence); $r_o = 11.8$ cm, and $\sigma_R^2 = 0.11$. Solid curve, prediction from Rytov's theory with Eq. (4).

pect, the agreement between Rytov theory and the numerical results is quite good.

3. RESULTS

Our principal results are shown in Figs. 3 and 4, where σ_I^2 and the aperture-averaged irradiance variance $\langle \sigma_I^2 \rangle$ are shown, respectively, as functions of the Rytov standard deviation σ_R . Open circles in the figures correspond to the HV-21 profile, solid circles correspond to the HA profile, and error bars indicate the variance's standard error as estimated from the four to seven computational runs. (As a point of reference, we note that $\sigma_R = 2$ for the HV-21 profile can be attained by attributing Γ solely to a 77° zenith-angle factor.) As a test, we performed several runs for a numerical model with five phase screens and found no statistically significant difference in the results. The dashed curve in Fig. 3 corresponds to $\sigma_I = \sigma_R$, and the solid curves are fits of the data to the empirical formula:

$$\sigma_I^2 = \sigma_o^2 [1 - \exp(-(\sigma_R^2/\sigma_o^2))]. \quad (5)$$

Here σ_o^2 is a parameter that indicates both the level of saturation in the strong-focusing regime and the Rytov variance where saturation sets in. It should be noted that Eq. (5) is not based on any underlying theory of scintillation; rather, it is simply a convenient analytical form for discussion of the numerical results.

Regarding Fig. 3, it is apparent that the two profiles display different saturation characteristics. Specifically, σ_I^2 for the HA profile in the strong-focusing regime is smaller than σ_I^2 for the HV-21 profile. In terms of Eq. (5) this may be summarized as $\sigma_o^2(\text{HA}) = 1.6$ and $\sigma_o^2(\text{HV-21}) = 2.5$. Regarding Fig. 4, we have the alternative finding that $\langle \sigma_I^2 \rangle$ in the saturation regime is smaller for the HV-21 profile and larger for the HA profile. These apparently contradictory results may be reconciled if the HV-21 profile produces a log-amplitude correlation function with a relatively short correlation length. A short correlation length implies not only significant amplitude fluctuations at a point from instant to instant (i.e., large σ_I^2 for the point intensity from realization to realization), but also a greater ability for the telescope aperture to average out amplitude fluctuations at any given instant (i.e., small $\langle \sigma_I^2 \rangle$). Figure 5 shows the log-amplitude correlation functions for the two profiles in

the case of $\sigma_R = 4.8$, and it is clear that the HV-21 profile has the shorter correlation length. Consequently, Figs. 3–5 are self-consistent and result in two immediate conclusions. First, the atmosphere's vertical turbulence profile has an important influence on the saturation of stellar scintillation. Second, the combination of high- and low-altitude turbulence is more effective in producing scintillation in the strong-focusing regime than high-altitude

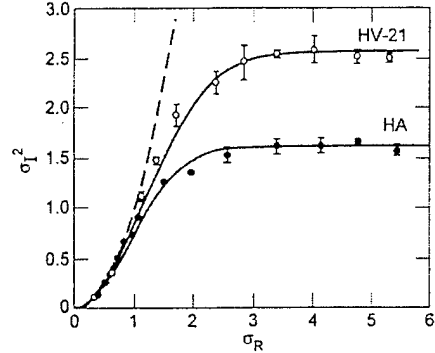


Fig. 3. Phase-screen calculation of irradiance variance σ_I^2 versus the Rytov standard deviation σ_R . Open circles, HV-21 model; solid circles, HA model. Dashed curve, Rytov theory [i.e., expression (1)]; solid curves, Eq. (5) with $\sigma_o^2 = 1.6$ and $\sigma_o^2 = 2.5$ for the HA and the HV-21 profiles, respectively.

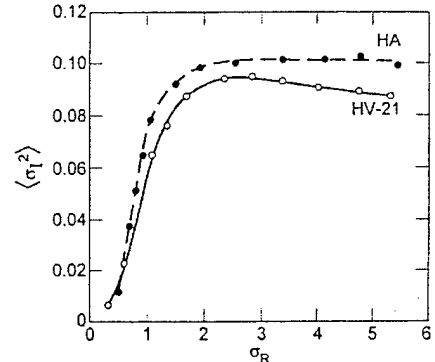


Fig. 4. Phase-screen calculation of the aperture-averaged irradiance variance $\langle \sigma_I^2 \rangle$ versus the Rytov standard deviation σ_R . Open circles, HV-21 model; solid circles, HA model. The telescope diameter in the simulations was 25 cm.

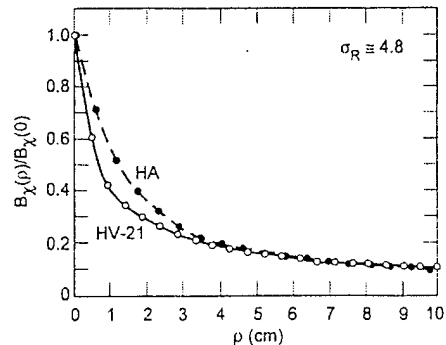


Fig. 5. Log-amplitude correlation function $B_X(\rho)/B_X(0)$ in the strong-focusing regime (i.e., $\sigma_R = 4.8$): open circles, HV-21 profile; solid circles, HA profile.

turbulence alone. We present a physical explanation for these conclusions in the next section.

4. DISCUSSION

As a way to explain scintillation qualitatively,¹⁶ turbulent eddies are often imagined as extremely long focal length lenses that randomly focus and defocus a coherent wave. For eddies of size l at an altitude h , the focal length varies like $\pm l^{2/3}/C_n(h)$. Moreover, in the regime of weak turbulence, where the effects of the individual eddies are independent, the variance of the fluctuations scales like the number of eddies along the propagation path. Thus, not only do small eddies produce the greatest intensity fluctuations at the point of observation, but also there are more of them along the propagation path. Taken together, these statements imply that the smallest-scale eddies dominate the production of scintillation. Of course, the smallest eddy that can efficiently focus or defocus the light in this fashion is constrained by diffraction, which limits the smallest-scale eddies of relevance for scintillation to the Fresnel length.

While the above description of scintillation is appropriate in the regime of weak turbulence, and in fact provides a semiquantitative rationale for the Rytov variance's form, it lacks an important subtlety.^{17,18} In the regime of strong turbulence a wave is perturbed by its propagation through the turbulent atmosphere before interacting with a Fresnel-scale eddy, with the consequence that this eddy must now focus or defocus a partially coherent field. Because the lateral coherence length ρ_o of a propagated field decreases as the path-integrated turbulence increases, a point is eventually reached at which the coherence length becomes smaller than the Fresnel length. At this level of turbulence, the Fresnel scale eddies lose their ability to effectively focus or defocus the wave. Consequently, further increases in turbulence do not produce much increase in scintillation, and the irradiance variance saturates.

In the present problem, as suggested by Eq. (1) and Fig. 1, the most significant Fresnel length for scintillation is associated with the tropopause for both the HA and the HV-21 profiles. Consequently, scintillation should saturate when the field's coherence length after propagation from space to the tropopause becomes smaller than the tropopause Fresnel length [i.e., $\rho_o(h) < \sqrt{\lambda h} \approx 10$ cm, assuming a 1- μ m wavelength and a 10-km tropopause altitude]. Clearly, the HA profile has more stratospheric turbulence than the HV-21 profile. Thus, for the same degree of weighted, path-integrated turbulence from space to Earth (i.e., σ_R), the HA profile will always produce a smaller coherence length at the tropopause, and this in turn implies that the HA profile will saturate at lower values of σ_R .

This argument can be placed on a more quantitative footing by writing the coherence length at an altitude h for a wave propagating from space to Earth as¹⁹

$$\rho_o(h) = \left[1.45 k^2 \int_h^\infty C_n^2(h') dh' \right]^{-3/5}. \quad (6)$$

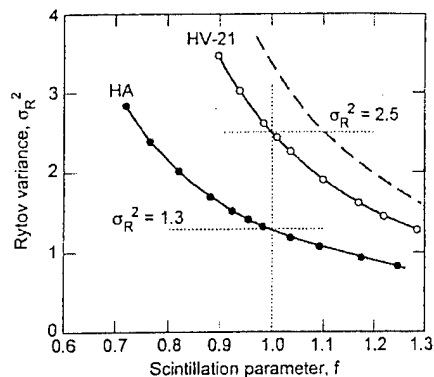


Fig. 6. Rytov variance parameterized by the scintillation parameter f as discussed in the text. Open circles, HV-21 profile with f averaged over the tropopause; solid circles, HA profile with f averaged over the tropopause; dashed curve, HV-21 profile with f averaged over the lower troposphere. For the tropopause-averaged curves, the HV-21 and the HA profile Rytov variances at $f = 1$ are in reasonable agreement with their respective σ_o^2 values.

Forming the ratio of $\rho_o(h)$ with the Fresnel length and then averaging over the tropopause region defines a scintillation-saturation parameter f :

$$f \equiv \frac{1}{h_2 - h_1} \int_{h_1}^{h_2} \left[\frac{\rho_o(h)}{\sqrt{\lambda h}} \right] dh, \quad (7)$$

where h_2 and h_1 correspond to the top and bottom of the tropopause, respectively. When f is less than unity for some vertical turbulence profile, the tropopause coherence length is less than the Fresnel length, and scintillation should saturate. Parametrizing the Rytov variance by f and writing this as $\sigma_R(f)$, we then expect σ_I^2 to saturate at $\sigma_R^2(1)$.

Figure 6 shows $\sigma_R^2(f)$ versus f for the HV-21 profile (open circles) and the HA profile (solid circles). As is clear from the figure, $\sigma_R^2(1)$ for the HA profile is smaller than $\sigma_R^2(1)$ for the HV-21 profile, consistent with the observation that σ_I^2 saturates at lower values for the HA profile. Moreover, we obtain $\sigma_R^2(1) = 2.5$ for the HV-21 profile and $\sigma_R^2(1) = 1.3$ for the HA profile, which are values that are consistent with $\sigma_o^2(\text{HV-21})$ and $\sigma_o^2(\text{HA})$, respectively. For completeness, the dashed curve in the figure shows σ_R^2 versus f for the HV-21 profile, but now with f averaged over the lower troposphere (i.e., 1–2.5 km). Comparison of the two HV-21 curves illustrates, that saturation is primarily associated with the tropopause for this profile, even though Fig. 1 suggests that the lower troposphere plays a significant scintillation role in the regime of weak turbulence.

5. SUMMARY

In this work we investigated the relationship between stellar scintillation in the strong-focusing regime and the atmosphere's vertical turbulence profile. Specifically, using the Hufnagel-Valley (HV-21) model of atmospheric turbulence, we compared the irradiance variance for the standard HV-21 turbulence profile with σ_I^2 values obtained from what we termed a high-altitude (i.e., HA) profile. In the HV-21 profile, scintillation arises from both

low- and high-altitude turbulence, while in the HA profile scintillation is dominated by high-altitude turbulence alone. Comparing the σ_I^2 values for the two profiles, which were obtained by numerical simulation, we found that in the strong-focusing regime the vertical profile of turbulence plays an important role in scintillation. Moreover, we found that the combination of high- and low-altitude turbulence was more effective in producing scintillation in the strong-focusing regime than high-altitude turbulence alone. These results were explained as a consequence of an optical wave's decoherence, relative to the tropopause Fresnel length, as it propagates through the lower stratosphere.

APPENDIX A

In the numerical simulation of optical propagation, the placement and strength of the phase screens is determined by a Gaussian quadrature procedure.²⁰ Basically, since we need to replace the continuous vertical turbulence profile with a set of discrete turbulent layers, we approximate the integral of C_n^2 with a discrete sum of N_s phase screens by using Gauss-Legendre quadrature:²¹

$$\int_0^H C_n^2(h)dh = \int_0^{0.3 \text{ km}} C_n^2(h)dh + \int_{0.3 \text{ km}}^H C_n^2(h)dh$$

$$= a_1 C_n^2(h_1) + \sum_{i=2}^{N_s} a_i C_n^2(h_i). \quad (\text{A1})$$

Here, H corresponds to a somewhat arbitrary 20 km height of the atmosphere, h_1 equals 0.15 km, and the h_i and a_i in the second term on the right-hand side of Eq. (A1) are obtained from standard tables²² [a_1 is just the integral of $C_n^2(h)$ over the lowest 300 meters of the atmosphere normalized to $C_n^2(h_1)$]. Table 1 shows the values of h_i determined by Gauss-Legendre quadrature for a four-screen model and a five-screen model. It should be noticed that the lowest phase screen is always placed at an altitude of 150 m to ensure sampling of boundary layer turbulence. (While this may not be particularly crucial for an investigation of stellar scintillation, it nevertheless seemed prudent to account for it in the simulation.) The strength of turbulence for the various phase screens may then be parameterized by a set of Fried parameters $\{r_{o,i}\}$:

$$r_{o,i}^{-5/3} = 0.423k^2 a_i C_n^2(h_i). \quad (\text{A2})$$

Once the $\{r_{o,i}\}$ is determined, a set of random phase screens is generated with Fried's methodology.²³ Briefly, on a square $M \times M$ pixel screen we generate M^2 mean-zero, delta-correlated, Gaussian random variables, $w(m_x, m_y) = w(\mathbf{m})$, with a variance of α^2 . The two-dimensional discrete Fourier transform of $w(\mathbf{m})$, $W(\boldsymbol{\eta})$, is then multiplied by $|\boldsymbol{\eta}|^{-11/6}$ (except at $|\boldsymbol{\eta}| = 0$, where $W(\boldsymbol{\eta})$ is set equal to zero) to produce a random field with a Kolmogorov spectrum. Taking the inverse Fourier transform of $W(\boldsymbol{\eta})|\boldsymbol{\eta}|^{-11/6}$ yields $\theta_{\text{TTE}}(\mathbf{m})$, the random phase field with uncorrected tip and tilt (to be discussed below). The variance α^2 is chosen so that the structure function associated with $\theta_{\text{TTE}}(\mathbf{m})$ matches that determined by the Fried parameter $r_{o,i}$: $\alpha_i = CM(L/r_{o,i})^{5/6}$, where L is the length of the phase screen and $C \approx 0.1513128$.

Table 1. Altitudes of Phase Screens

Screen Number	h_i for 4-Screens [km]	h_i for 5-Screens [km]
1	0.15	0.15
2	2.52	1.67
3	10.15	6.80
4	17.78	13.5
5		18.63

In generating the random phase field, $\theta_{\text{TTE}}(\mathbf{m})$, we employ a screen of finite size. However, strict homogeneity of the random field requires a screen of infinite dimension, implying that the lowest-order Fourier components of $\theta_{\text{TTE}}(\mathbf{m})$ (i.e., tip and tilt) are likely to be in error. A similar problem exists in the simulation of a random time series, where initiation of the series results in a nonstationary random process.²⁴ Fried corrects this error by subtracting the incorrect tip and tilt from $\theta_{\text{TTE}}(\mathbf{m})$ and then adding a statistically appropriate degree of tip and tilt:

$$\theta(\mathbf{m}, h_i) = \theta_{\text{TTE}}(\mathbf{m})$$

$$- \boldsymbol{\beta} \cdot \left(\mathbf{m} - \frac{M}{2} \mathbf{I} \right) + \gamma \mathbf{g} \cdot \left(\mathbf{m} - \frac{M}{2} \mathbf{I} \right). \quad (\text{A3})$$

Here, $\theta(\mathbf{m}, h_i)$ is the random phase screen employed in the computations, \mathbf{I} is a unit vector, \mathbf{g} is a normal random vector (with mean-zero and unit-variance components), γ is the standard deviation of the statistically appropriate tip and tilt vector, and $\boldsymbol{\beta}$ is the erroneous tip and tilt vector:

$$\boldsymbol{\beta} = \frac{12}{M^2(M^2 - 1)} \sum_{\mathbf{m}=1}^M \left(\mathbf{m} - \frac{(M+1)}{2} \mathbf{I} \right) \theta_{\text{TTE}}(\mathbf{m}). \quad (\text{A4})$$

Fried derives the statistically appropriate variance of tip and tilt from the phase structure function: $\gamma_i \approx 2.610111/M(L/r_{o,i})^{5/6}$.

Though the methodology of Fried ensures that each phase screen can approximate an appropriate stochastic scalar field, Knepp²⁵ has pointed out that numerical aspects of the simulation problem must also be considered in order to obtain realistic results. From the form of the phase structure function for the i th screen, we have $D_{\theta,i}(\delta r) = 6.884(\delta r/r_{o,i})^{5/3}$, where δr is the phase screen's pixel size: $\delta r = L/M$. Clearly, if the screen is to accurately represent turbulent refractive index fluctuations, then the phase variations from pixel to pixel should be less than 90° . We achieve this constraint by requiring $D_{\theta,i}(2\delta r) < (\pi/2)^2$, which implies an upper bound on δr that is determined by the $r_{o,i}$. Since $r_{o,i}$ is always larger than r_o , where $r_o^{-5/3} = \sum_i r_{o,i}^{-5/3}$, we get a criterion for the pixel size: $\delta r < (r_o/2)(\pi^2/27.54)^{3/5}$; this may be called the structure-function criterion on the pixel size. Additionally, if scintillation in the saturation regime is to be accurately simulated, then the pixel size should also be less than the Fresnel length associated with interscreen propagation: $\delta r < \frac{1}{2}(\lambda \Delta z_s)^{1/2}$, where Δz_s is the smallest interscreen distance; this may be called the interscreen-

Fresnel-length criterion on the pixel size. The smaller of these two criteria places an upper limit on the pixel size. In the present simulations, we found that the upper bound on δr for the HA profile was determined by the interscreen-Fresnel-length criterion, and was relatively insensitive to our wind speed changes in turbulence. However, for the HV-21 profile, δr was primarily determined by the structure-function criterion and did change with Γ from a maximum of 0.4 cm to a minimum of 0.3 cm. Note that as a general rule the structure-function criterion scales like $\lambda^{6/5}$, whereas the interscreen-Fresnel-length criterion scales like $(\lambda/N_s)^{1/2}$.

In addition to an upper bound on the pixel size, there is also a lower bound. As mentioned above, wave propagation between phase screens is accomplished by Fourier transform and the Fresnel approximation. Specifically, if $\psi(h)$ is the two-dimensional Fourier transform of the field at h , then

$$\psi(h_2) = \psi(h_1) \exp\left[-\frac{i\kappa^2(h_1 - h_2)}{2k}\right], \quad (\text{A5})$$

where κ is the magnitude of spatial frequency. As the values of κ are discrete in the simulation (i.e., $\kappa_m = m\pi/L$, $m = 1, 2, \dots, M$), an accurate description of propagation with use of the Fourier transformation requires that the difference in phase associated with the two largest values of κ be small compared with π :

$$\frac{M^2\pi^2\Delta z}{2kL^2} - \frac{(M-1)^2\pi^2\Delta z}{2kL^2} < \pi, \quad (\text{A6})$$

where $\Delta z = (h_1 - h_2)$. When we define Δz_L as the largest separation between phase screens, Eq. (7) results in a lower bound on δr : $\delta r > (\lambda\Delta z_L/2M)^{1/2}$. Note that together, the upper and lower bounds on δr constrain the range of investigations that may be performed for a given number of pixels, M . Under conditions where the upper bound on δr is determined by the interscreen-Fresnel-length criterion, M must be greater than $(2\Delta z_L/\Delta z_s)$, whereas under conditions where δr 's upper bound is fixed by the structure-function criterion, M must be greater than $(6.85\lambda\Delta z_L/r_o^2)$. If these constraints on M are violated, then there is no value of δr that satisfies both the upper and lower bounds, and calculation can proceed only with an increased value of M .

Finally, because of the finite size of the phase screen, the Fourier transform of the propagated field is periodic, and this can lead to spurious interference effects near the screens' edges. To clarify this problem, define $E(\rho_{\text{edge}}^+, h_1)$ as a field element at the plus or minus transverse side of an upper-altitude phase screen. Due to the turbulent eddies in the upper screen, the plus field element may (for example) scatter outside the footprint of a lower-altitude screen, whereas the minus field element may stay within the footprint. However, as a consequence of the Fourier transform's periodic nature, the plus field element is not lost in the calculation but reappears at the opposite edge of the lower-altitude screen as a spurious field element [i.e., $E(\rho_{\text{edge}}^+, h_1) \rightarrow \bar{E}_{\text{sp}}(\rho_{\text{edge}}^-, h_2)$, while $E(\rho_{\text{edge}}^-, h_1) \rightarrow \bar{E}(\rho_{\text{edge}}^+, h_2)$]. The total field at the minus side of the lower-altitude screen is the sum of the propagated minus-side field ele-

ment plus the spurious field element: $E(\rho_{\text{edge}}^-, h_2) = \bar{E}(\rho_{\text{edge}}^-, h_2) + \bar{E}_{\text{sp}}(\rho_{\text{edge}}^-, h_2)$. Since the field elements at opposite edges of a screen should be only weakly correlated (if at all), this effect not only results in spurious partial destructive interference at the screen edges but also introduces a spurious correlation into the propagated field at the screen edges. To guard against these edge effects, we first estimate the interscreen scattering angle for propagation from screen i to screen $i+1$, ϕ_i : $\sin(\phi_i) \equiv (ks_{o,i})^{-1}$, where $s_{o,i}$ is defined by $D_{\theta,i}(s_o) = 1$. The range in transverse dimension near the $i+1$ screen's edge that is corrupted by periodicity of the Fourier transform is then approximately $(h_i - h_{i+1})(ks_{o,i})^{-1}$. Adding the corrupted ranges for all the screens provides an apodizing radius, r_a , at the telescope aperture: $r_a = L/2 - \sum_{i=1}^{N_s-1} (h_i - h_{i+1})/ks_{o,i}$. As long as $2r_a$ is larger than the telescope aperture's diameter, these edge effects should have little influence on the results.

ACKNOWLEDGMENTS

The author is grateful to H. Yura for many useful and enlightening discussions throughout the course of this work as well as for a critical reading of the manuscript. The author also thanks S. C. Moss and G. Valley for critical readings of the manuscript and useful comments regarding its improvement. This work was supported under U.S. Air Force Contract F04701-93-C-0094.

REFERENCES AND NOTES

1. R. R. Beland, "Propagation through atmospheric optical turbulence," in *Atmospheric Propagation of Radiation*, F. G. Smith, ed. (SPIE Press, Bellingham, Wash., 1993), Chap. 2.
2. V. I. Tatarski, *Wave Propagation in a Turbulent Medium* (McGraw-Hill, New York, 1961), Chap. 8.
3. M. E. Gracheva, A. S. Gurvich, S. S. Kashkarov, and V. V. Pokasov, "Similarity relations and their experimental verification for strong intensity fluctuations of laser radiation," in *Laser Beam Propagation in the Atmosphere*, J. W. Strohbehn, ed. (Springer-Verlag, Berlin, 1978), Chap. 4.
4. A. Consortini, F. Cochetti, J. H. Churnside, and R. J. Hill, "Inner-scale effect on irradiance variance measured for weak-to-strong atmospheric scintillation," *J. Opt. Soc. Am. A* **10**, 2354-2362 (1993).
5. S. M. Flatté, G.-Y. Wang, and J. Martin, "Irradiance variance of optical waves through atmospheric turbulence by numerical simulation and comparison with experiment," *J. Opt. Soc. Am. A* **10**, 2363-2370 (1993).
6. S. M. Flatté, C. Bracher, and G.-Y. Wang, "Probability-density functions of irradiance for waves in atmospheric turbulence calculated by numerical simulation," *J. Opt. Soc. Am. A* **11**, 2080-2092 (1994); R. Hill and R. G. Frehlich, "Probability distribution of irradiance for the onset of strong scintillation," *J. Opt. Soc. Am. A* **14**, 1530-1540 (1997).
7. D. Dravins, L. Lindegren, E. Mezey, and A. T. Young, "Atmospheric intensity scintillation of stars. I. Statistical distributions and temporal properties," *Publ. Astron. Soc. Pac.* **109**, 173-207 (1997).
8. J. Bufton and S. H. Genatt, "Simultaneous observations of atmospheric turbulence effects on stellar irradiance and phase," *Astron. J.* **76**, 378-386 (1971); see also G. Parry, J. G. Walker, and R. J. Scaddan, "On the statistics of stellar speckle patterns and pupil plane scintillation," *Opt. Acta* **26**, 563-574 (1979).
9. In the following, we refer to the lower 9 km of atmosphere

- as the troposphere, the 9–12-km region as the tropopause, and the 12–20-km region as the lower stratosphere.
10. H. A. Whale, "Diffraction of a plane wave by a random phase screen," *J. Atmos. Terr. Phys.* **35**, 263–274 (1973); R. Buckley, "Diffraction by a random phase-changing screen: a numerical experiment," *J. Atmos. Terr. Phys.* **37**, 1431–1446 (1975); W. P. Brown, "Computer simulation of adaptive optical systems," Hughes Research Laboratories Report, contract N60921–74–C–0249, 1975; B. L. McGlamery, "Computer simulation studies of compensation of turbulence degraded images," in *Image Processing*, J. C. Urbach ed., Proc. SPIE **74**, 225–233 (1976).
 11. J. M. Martin and S. M. Flatté, "Intensity images and statistics from numerical simulation of wave propagation in 3-D random media," *Appl. Opt.* **27**, 2111–2126 (1988); W. A. Coles, J. P. Filice, R. G. Frehlich, and M. Yadlowsky, "Simulation of wave propagation in three-dimensional random media," *Appl. Opt.* **34**, 2089–2101 (1995).
 12. J. W. Goodman, *Introduction to Fourier Optics* (McGraw-Hill, San Francisco, Calif., 1968).
 13. For completeness, we note that the pixel size of ~ 0.3 cm– 0.4 cm introduces an inner scale of turbulence into the simulations. This is an unavoidable consequence of all finite element numerical simulations.
 14. In principle, a telescope of any diameter may be simulated. However, for larger-aperture telescopes to be considered, the phase-screen length must also become larger, which in turn requires a larger number of pixels to span the screen's length. (As discussed in Appendix A, the pixel size is bounded by considerations related to the strength of turbulence and the interscreen spacing.) The computational requirements for dealing with phase screens that have large numbers of pixels can quickly become prohibitive.
 15. William L. Hays, *Statistics* (Holt, Rinehart & Winston, New York, 1988), Chap. 5.
 16. J. W. Strohbehn, "Modern theories in the propagation of optical waves in a turbulent medium," in *Laser Beam Propagation in the Atmosphere*, J. W. Strohbehn ed. (Springer-Verlag, Berlin, 1978), Chap. 3.
 17. H. T. Yura, "Physical model for strong optical-amplitude fluctuations in a turbulent medium," *J. Opt. Soc. Am.* **64**, 59 (1974).
 18. S. F. Clifford, G. R. Ochs, and R. S. Lawrence, "Saturation of optical scintillation by strong turbulence," *J. Opt. Soc. Am.* **64**, 148–154 (1974).
 19. R. E. Hufnagel and N. R. Stanley, "Modulation transfer function associated with image transmission through turbulent media," *J. Opt. Soc. Am.* **54**, 52–61 (1964).
 20. S. E. Troxel, R. M. Welsh, and M. C. Roggemann, "Off-axis optical transfer function calculations in an adaptive-optics system by means of a diffraction calculation for weak index fluctuations," *J. Opt. Soc. Am. A* **11**, 2100–2111 (1994).
 21. C-E. Fröberg, *Introduction to Numerical Analysis* (Addison-Wesley, Reading, Mass., 1965), Chap. 10.
 22. M. Abramowitz and I. A. Stegun, *Handbook of Mathematical Functions*, (Dover, New York, 1972), Chap. 25.
 23. The author received the text of D. Fried's phase-screen generation algorithm from D. L. Fried, 14671 Tumbleweed Lane, Monterey County, Calif. 95076 (private communication).
 24. M. J. Levin, "Generation of a sampled Gaussian time series having a specified correlation function," *IRE Trans. Inf. Theory* **IT-6**, 545–548 (1960); J. C. Camparo and P. Lambropoulos, "Monte Carlo simulations of field fluctuations in strongly driven resonant transitions," *Phys. Rev. A* **47**, 480–494 (1993).
 25. D. L. Knepp, "Multiple phase-screen calculation of the temporal behavior of stochastic waves," *Proc. IEEE* **71**, 722–737 (1983).

LABORATORY OPERATIONS

The Aerospace Corporation functions as an "architect-engineer" for national security programs, specializing in advanced military space systems. The Corporation's Laboratory Operations supports the effective and timely development and operation of national security systems through scientific research and the application of advanced technology. Vital to the success of the Corporation is the technical staff's wide-ranging expertise and its ability to stay abreast of new technological developments and program support issues associated with rapidly evolving space systems. Contributing capabilities are provided by these individual organizations:

Electronics and Photonics Laboratory: Microelectronics, VLSI reliability, failure analysis, solid-state device physics, compound semiconductors, radiation effects, infrared and CCD detector devices, data storage and display technologies; lasers and electro-optics, solid state laser design, micro-optics, optical communications, and fiber optic sensors; atomic frequency standards, applied laser spectroscopy, laser chemistry, atmospheric propagation and beam control, LIDAR/LADAR remote sensing; solar cell and array testing and evaluation, battery electrochemistry, battery testing and evaluation.

Space Materials Laboratory: Evaluation and characterizations of new materials and processing techniques: metals, alloys, ceramics, polymers, thin films, and composites; development of advanced deposition processes; nondestructive evaluation, component failure analysis and reliability; structural mechanics, fracture mechanics, and stress corrosion; analysis and evaluation of materials at cryogenic and elevated temperatures; launch vehicle fluid mechanics, heat transfer and flight dynamics; aerothermodynamics; chemical and electric propulsion; environmental chemistry; combustion processes; space environment effects on materials, hardening and vulnerability assessment; contamination, thermal and structural control; lubrication and surface phenomena.

Space Science Application Laboratory: Magnetospheric, auroral and cosmic ray physics, wave-particle interactions, magnetospheric plasma waves; atmospheric and ionospheric physics, density and composition of the upper atmosphere, remote sensing using atmospheric radiation; solar physics, infrared astronomy, infrared signature analysis; infrared surveillance, imaging, remote sensing, and hyperspectral imaging; effects of solar activity, magnetic storms and nuclear explosions on the Earth's atmosphere, ionosphere and magnetosphere; effects of electromagnetic and particulate radiations on space systems; space instrumentation, design fabrication and test; environmental chemistry, trace detection; atmospheric chemical reactions, atmospheric optics, light scattering, state-specific chemical reactions and radiative signatures of missile plumes.

Center for Microtechnology: Microelectromechanical systems (MEMS) for space applications; assessment of microtechnology space applications; laser micromachining; laser-surface physical and chemical interactions; micropropulsion; micro- and nanosatellite mission analysis; intelligent microinstruments for monitoring space and launch system environments.

Office of Spectral Applications: Multispectral and hyperspectral sensor development; data analysis and algorithm development; applications of multispectral and hyperspectral imagery to defense, civil space, commercial, and environmental missions.



2350 E. El Segundo Boulevard
El Segundo, California 90245-4691
U.S.A.